Inorganic Chemistry

pubs.acs.org/IC Article

The Synthesis of a Quasi-One-Dimensional Iron-Based Telluride with Antiferromagnetic Chains and a Spin Glass State

Jun Zhang,[▽] Lei Duan,[▽] Zhe Wang,[▽] Xiancheng Wang,* Jianfa Zhao, Meiling Jin, Wenmin Li, Changling Zhang, Lipeng Cao, Zheng Deng, Zhiwei Hu, Stefano Agrestini, Manuel Valvidares, Hong-Ji Lin, Chien-Te Chen, Jinlong Zhu,* and Changqing Jin*

Cite This: *Inorg. Chem.* 2020, 59, 5377−5385 Read Online

ACCESS | Metrics & More | Article Recommendations | Supporting Information

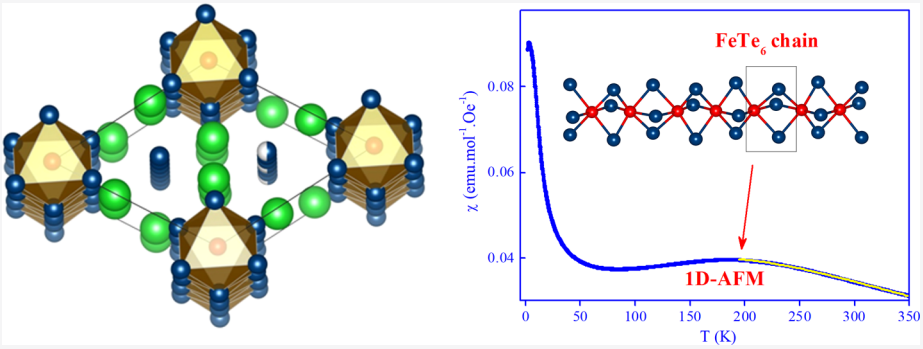

ABSTRACT: The report on the superconductivity of the two-legged spin ladders $BaFe_2S_3$ and $BaFe_2Se_3$ has established 123-type iron chalcogenides as a novel subgroup in the iron-based superconductor family and has stimulated the continuous exploration of other iron-based materials with new structures and potentially novel properties. In this paper, we report the systematic study of a new quasi-one-dimensional (1D) iron-based compound, $Ba_9Fe_3Te_{15}$, including its synthesis and magnetic properties. The high-pressure synthesized $Ba_9Fe_3Te_{15}$ crystallized in a hexagonal structure that mainly consisted of face-sharing $FeTe_6$ octahedral chains running along the c axis, with a lattice constant of a = 10.23668 Å; this led to weak interchain coupling and an enhanced one-dimensionality. The systematic static and dynamic magnetic properties were comprehensively studied experimentally. The dc magnetic susceptibility showed typical 1D antiferromagnetic characteristics, with a T_{max} at 190 K followed by a spin glass (SG) state with freezing at $T_f \approx 6.0$ K, which were also unambiguously proved by ac susceptibility measurements. Additionally, X-ray magnetic circular dichroism (XMCD) experiments revealed an unexpected orbital moment for Fe^{2+}, i.e., 0.84 μ_B per Fe in $Ba_9Fe_3Te_{15}$. The transport property is electrically insulating, with a thermal activation gap of 0.32 eV. These features mark $Ba_9Fe_3Te_{15}$ as an alternative type of iron-based compound, providing a diverse candidate for high-pressure studies in order to pursue some emerging physics.

1. INTRODUCTION

The design and exploration of materials in order to pursue unique physical properties is always challenging. However, some similar structural features are shared among the many systems being investigated. For instance, the iron-based superconductors that have been discovered so far include the FeX_4 motif (where X represents pnictogens or chalcogens), where the iron ions are generally positively divalent despite having different connections in the 2D-layered or quasi-1D ladder-type systems.[1−6] Nevertheless, some compounds with the same $FeAs_4$ tetrahedral geometry as the local structural units but with a three-dimensional spatial arrangement, such as $CaFe_4As_3$, have antiferromagnetic (AFM) long-range ordering without superconductivity down to 1.8 K.[7] Additionally, Ba_2FeS_3, consisting of corner-sharing FeS_4 tetrahedra that form an infinite linear chain, has not been reported to be superconducting to date.[8] From a crystal structure perspective, not only the local building unit but also the dimensionality undoubtedly influences the physical properties by strongly influencing the Fermi surface topology and magnetic ground state.[9]

Although extensive studies have focused on the interplay among the crystal structure, magnetism, and electrons, the superconductivity mechanism and its relationship to the crystal

Received: December 10, 2019
Published: April 3, 2020

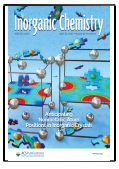

https://dx.doi.org/10.1021/acs.inorgchem.9b03592
Inorg. Chem. 2020, 59, 5377−5385

structure motifs in these systems are still debated. Thus, more iron-based compounds with different geometry arrangements are actively being sought in order to clarify the potential mechanism and to pursue a higher T_c. Since the first report of superconductivity in the quasi-1D 123-type iron chalcogenide with a two-legged iron ladder,[4] the 1D structure has been paid more attention. However, other 1D systems with infinite linear iron chains, such as $Ba_9Fe_3X_{15}$ (where X denotes S, Se, and Te), have been less explored until now. $Ba_9Fe_3S_{15}$ is an interesting compound that displays a quasi-1D crystal structure consisting of face-sharing FeS_6 octahedral chains and S chains.[10] Its magnetic and electronic properties prove that the ferrimagnetic ground state derives from the strong coupling interactions between neighboring iron ions running along the 1D direction, and that semiconductor behavior is due to less electron hopping between adjacent chains and to the strong electronegativity of the S atoms.[11] As the anion evolves from S to Te, the increased ion radius is expected to weaken the neighboring Fe−Fe coupling interactions along the 1D chain, causing an antiferromagnetic correlation interaction in $Ba_9Fe_3Te_{15}$. In addition, compared to $Ba_9Fe_3S_{15}$ and $Ba_9Fe_3Se_{15}$, the more extended 5p orbital of the Te ion in $Ba_9Fe_3Te_{15}$ enhances the interchain electronic hopping and increases the conductivity. Thus, the telluride is always distinguishable from the other chalcogenides. For example, the theoretical works showed that hexagonal FeTe with octahedral $FeTe_6$ is much less magnetic than hexagonal FeS and FeSe. Therefore, unconventional magnetically mediated superconductivity is possible in hexagonal FeTe.[12] Furthermore, it has been reported that the self-doping mechanism caused by electrons transferring from S to Fe in $BaFe_2S_3$ plays a key role in the superconductivity transition, similar to the layered iron superconductors where the high electron density of Fe also helps to quench the magnetic moment and realize the magnetic-to-nonmagnetic transition before becoming superconducting.[13]

$Ba_9Fe_3Te_{15}$ has face-sharing octahedral $FeTe_6$ chains and is expected to exhibit both antiferromagnetic correlation and increased conductivity, which makes it a good candidate for research into unconventional magnetically mediated superconductivity in the quasi-1D chain systems. Further, compared to sulfide, the increased covalence between the Fe and the Te atoms due to the much weaker electronegativity in the Te atoms helps contribute to the higher electronic density of Fe, which favors inducing superconductivity under relatively mild conditions. In this work, the iron-based telluride $Ba_9Fe_3Te_{15}$ with a quasi-1D structure was initially synthesized, where the iron was coordinated by six tellurium atoms, and showed a different crystal structure and microstructure compared to the previously discovered iron-based superconductors. Magnetic property measurements found an unexpected orbital moment of ∼0.84 μ_B per Fe and typical one-dimensional antiferromagnetic characteristics, followed by a spin glass state at 6.0 K that was verified by static and dynamic magnetic studies. The transport property behaves as a semiconductor with a thermal activation gap of ∼0.32 eV, which is somewhat similar to that observed in the 123-type iron chalcogenides.[4,5,14] All of these features suggest that $Ba_9Fe_3X_{15}$ (where X denotes S, Se, and Te) could be a new subgroup that enriches the iron-based family.

2. EXPERIMENTAL SECTION

2.1. Sample Synthesis. A $Ba_9Fe_3Te_{15}$ polycrystalline sample was synthesized by employing a solid state reaction at high-pressure and high-temperature conditions. Commercially available lumps of Ba (Alfa, immersed in oil, >99.2% pure) and crystalline powders of Fe (Alfa, 99.998% pure) and Te (Alfa, >99.999% pure) were used as the starting materials. BaTe was first prepared by heating the mixture of Ba blocks and Te powder in an evacuated quartz tube at 600 °C for 10 h. The mixture of BaTe, Fe, and Te powders with a stoichiometric proportion of 3:1:2 was finely ground and pressed into a flake, which was then sintered at 1200 °C and 5.5 GPa for 30 min. The $Ba_9Fe_3Te_{15}$ powder sample was obtained and then quenched to room temperature for further experiments.

2.2. Characterizations. Powder X-ray diffraction (XRD) was performed on a Rigaku Ultima VI (3KW) diffractometer using Cu Kα radiation generated at 40 kV and 40 mA. The X-ray diffraction data were collected with a scanning rate of 1° per minute and a scanning step length of 0.02°. The Rietveld refinement of the diffraction spectra was carried out with the GSAS software packages.[15] The dc magnetic susceptibility was measured with a superconducting quantum interference device (SQUID). The electric transport property was measured using the standard four-probe method with a physical property measuring system (PPMS). The PPMS was also used for thermodynamic property and ac susceptibility measurements; the ac susceptibility was under a zero dc background field with an amplitude of 8 Oe for different frequencies. The X-ray absorption spectroscopy (XAS) and X-ray magnetic circular dichroism (XMCD) measurements of the Fe-$L_{2,3}$ edges were performed at the beamline BOREAS of synchrotron ALBA in Barcelona with a degree of circular polarization close to 100%.[16] The sample was fractured in situ in order to obtain a clean surface and was measured at 25 K in a magnetic field of 6 T using the total electron yield method.

3. RESULTS AND DISCUSSION

The XRD pattern of $Ba_9Fe_3Te_{15}$, measured at room temperature, and the corresponding structural refinement results are shown in Figure 1. Based on the Rietveld analysis, the as-

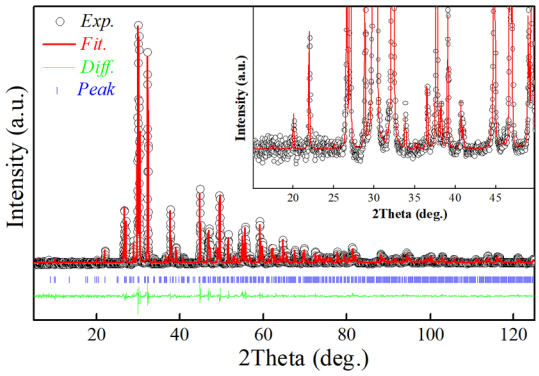

Figure 1. X-ray diffraction pattern of $Ba_9Fe_3Te_{15}$, measured at room temperature, together with its structural refinement. The inset shows the enlarged view at the low angle region. The observed (black circles), calculated (red line), and difference (bottom line) values are shown. The ticks indicate the allowed Bragg reflections with space group $P\bar{6}c2$ (no. 188).

prepared $Ba_9Fe_3Te_{15}$ crystallizes to a hexagonal lattice and adopts the space group $P\bar{6}c2$ (no. 188), which is the same as its family compounds $Ba_9Fe_3S_{15}$,[10] $Ba_9Fe_3Se_{15}$,[17] $Ba_9Sn_3Te_{15}$, and $Ba_9V_3Se_{15}$ reported in our previous work.[18,19] Accordingly, all diffraction peaks for $Ba_9Fe_3Te_{15}$ can be well indexed and fitted according to the $P\bar{6}c2$ (no. 188) space group; no impurities are detected in the diffraction spectrum even in the enlarged scale of the Figure 1 inset, proving that the $Ba_9Fe_3Te_{15}$ sample is

https://dx.doi.org/10.1021/acs.inorgchem.9b03592
Inorg. Chem. 2020, 59, 5377−5385

highly pure. The compound has a trimeric structure due to the presence of a superlattice along the *c* axis, as detailed in Figure 2.

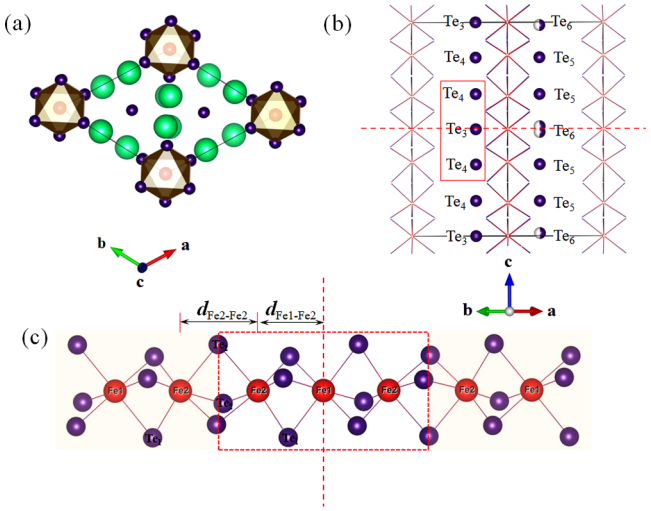

Figure 2. Schematic crystal structures: (a) the view along the [001] direction showing the hexagonal geometry arrangement; (b) the view from the [110] projection showing the Te chains running along the *c* axis (for clarity, Ba atoms are not shown); and (c) the $FeTe_6$ chain along the *c* axis. The solid and dashed line rectangles in (b) and (c) are used to emphasize the $-Te_4-Te_3-Te_4-$ and $-Fe_2-Fe_1-Fe_2-$ trimerizing units. The green spheres, red spheres, and dark blue spheres represent the Ba, Fe, and Te atoms, respectively.

The important crystallographic parameters, including the interatomic distances and angles, are summarized in Table 1. The lattice constants of $Ba_9Fe_3Te_{15}$ are $a = b = 10.2366(8)$ Å and $c = 19.8175(3)$ Å, and the crystal structure is illustrated in Figure 2. Figure 2a shows a projection down the *c* axis and illustrates the distorted hexagonal close-packed layers of Ba and Te. A triangular lattice is formed by the infinite columns of the face-sharing Te octahedron, and the interstices along the *c* axis are occupied by Fe. The Ba atoms are located in the interstices between the neighboring $FeTe_6$ octahedral columns. Therefore, the distance between the adjacent 1D Fe chains is given by the lattice constant *a*, i.e., 10.2366(8) Å. Figure 2b is a projection from the *ab* direction and shows the zigzag chains along the *c* axis. Parallel to the *c* axis, there are Te chains in the center of the trigonal channels. Further, it was found that the lattice parameter *c* is tripled due to the presence of a superlattice, including the $-Te_4-Te_3-Te_4-$ and $-Fe_2-Fe_1-Fe_2-$ trimerizing units in the Te chains and $FeTe_6$ octahedra columns, respectively. A mirror plane separating the Te_4-Te_4 and Te_5-Te_5 units on each side is shown in Figure 2b. Thus, the occupancy factor for Te_6 atoms is only 0.5, since the other symmetrical site at a distance of 0.53 Å is given by a 2-fold axis. The detailed microstructure of the $FeTe_6$ chain is shown in Figure 2c. There are two iron sites, named Fe_1 and Fe_2. The Fe_2 atoms are symmetrically arranged at each side of Fe_1 in a trimerizing unit because of the mirror plane reflection, leading to distinguishable bond lengths of $d_{Fe_1-Fe_2}$ and $d_{Fe_2-Te_2}$. The bond lengths in the $FeTe_6$ octahedron of $d_{Fe_1-Te_1}$, $d_{Fe_2-Te_1}$, and $d_{Fe_2-Te_2}$ are 2.961(8), 2.809(4), and 3.013(5) Å, respectively. Therefore, the $FeTe_6$ octahedra are slightly distorted, which is directly reflected by the bond angles of $\angle_{Te_1-Fe_1-Te_1}$ and $\angle_{Te_1-Fe_2-Te_2}$ being 177.94° and 169.86°, respectively, which deviate from 180° in an ideal octahedron. The bond length of Fe−Te changes from 2.5527(3) to 2.6148(1) Å as the coordination number increases from four to six.[20,21] Compared with these reported results, the bond lengths in $Ba_9Fe_3Te_{15}$ are longer; these results indicate a strong covalence between the Fe and Te ions, thereby causing the high electron density of Fe that helps to quench the magnetic moment and trigger superconductivity according to the self-doping mechanism in $BaFe_2S_3$.[13] In addition, the Te_3-Te_4 (3.2645 Å) and Te_5-Te_6 (2.9857 Å) distances in $Ba_9Fe_3Te_{15}$ can lead to the bond-forming Te_2^{2-} dimers, as observed in some polytellurides.[18] Based on the analysis above, $Ba_9Fe_3Te_{15}$ may be expressed as $(Ba^{2+})_9(Fe^{2+})_3(Te^{2-})_9(Te_2^{2-})_3$, in which the iron tends to be positively divalent.

Table 1. Crystal Structure Parameters of $Ba_9Fe_3Te_{15}$

formula: $Ba_9Fe_3Te_{15}$ | calculated unit cell formula weight: 3317.51(1) g/mol
crystal system: hexagonal | $Z = 2$
space group: $P\bar{6}c2$ (no. 188) | density: 6.12(6) g/cm^3
| $V = 1798.45(1)$ Å^3
crystal parameters: $a = 10.2366(8)$ Å; $c = 19.8175(3)$ Å | $R_p = 3.1(7)\%$; $R_{wp} = 4.5(7)\%$; $\chi^2 = 2.21(2)$

atom	wyck.	*x*	*y*	*z*	U_{iso}	occ.
Ba_1	12l	0.00068(1)	0.37505(8)	0.08116(9)	0.0126(9)	1
Ba_2	6k	0.38143(4)	0.38551(2)	1/4	0.0170(5)	1
Fe_1	2a	0	0	0	0.0589(6)	1
Fe_2	4g	0	0	0.15368(9)	0.0200(8)	1
Te_1	12l	0.23559(2)	0.24159(6)	0.08464(1)	0.0138(2)	1
Te_2	6k	0.00618(1)	0.23194(7)	1/4	0.0129(5)	1
Te_3	2c	1/3	2/3	0	0.0438(5)	1
Te_4	4h	1/3	2/3	0.16472(8)	0.0533 (5)	1
Te_5	4i	2/3	1/3	0.16409(4)	0.0025 (1)	1
Te_6	4i	2/3	1/3	0.01343(3)	0.0253(8)	0.5

$d_{Fe1-Te1}$	$d_{Fe2-Te2}$	$d_{Fe2-Te1}$	$d_{Fe1-Fe2}$	$d_{Fe1-Fe2}$
2.961(8)	3.013(5)	2.809(4)	3.055(6)	3.797(6)

$\angle_{Te1-Fe1-Te1}$	$\angle_{Te1-Fe2-Te2}$
177.94(1)	169.86(4)

https://dx.doi.org/10.1021/acs.inorgchem.9b03592
Inorg. Chem. 2020, 59, 5377−5385

As for the valence state of the Fe ion, further evidence was given by the soft X-ray absorption spectra at Fe-$L_{2,3}$, which is well-known to be sensitive to the Fe valence state.[22,23] As shown in Figure 3, the Fe-$L_{2,3}$ XAS spectrum of $Ba_9Fe_3Te_{15}$ is

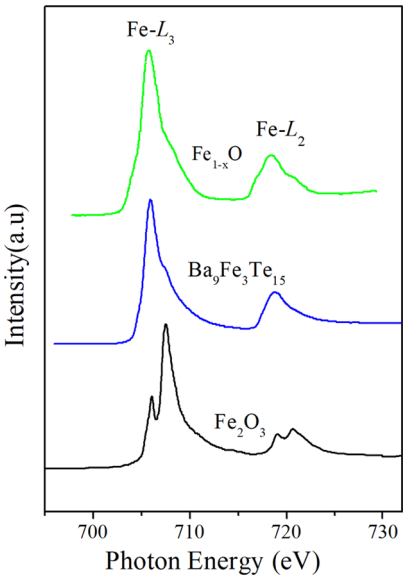

Figure 3. XAS of the Fe-$L_{2,3}$ edges for $Ba_9Fe_3Te_{15}$. Fe_2O_3 and $Fe_{1-x}O$ are used as references for comparison for Fe^{3+} and Fe^{2+}, respectively.

located at nearly the same photon energy as that of the Fe^{2+} reference $Fe_{1-x}O$[24] but is shifted by 1.6 eV to lower energies with respect to the Fe^{3+} reference Fe_2O_3. This confirms the Fe^{2+} valence state of $Ba_9Fe_3Te_{15}$,[25] which is consistent with the expectations for the formation of the Te_2^{2-} dimers. Although two sites are occupied by iron in the $-FeTe_6-$ chain, labeled Fe_1 and Fe_2, the XAS plot shows only one type of oxidation state and thus proves that both Fe_1 and Fe_2 are divalent. The Fe^{2+} is also a common characteristic for both two-dimensional layered square lattice and one-dimensional two-legged ladder iron-based superconductors.[1,4,6]

For an Fe^{2+} with a high spin configuration (S = 2), the theoretical spin-only effective moment is 4.9 μ_B per Fe, which could be effectively shown by the Curie–Weiss fitting of the inverse magnetic susceptibility. However, the temperature dependence of $1/\chi$ that was measured here does not obey a linear relationship when the temperature rises from 2 to 700 K, as shown in the inset of Figure 4a. The nonlinear behavior is possibly related to the thermal population of different excited states split by the strong spin–orbital coupling as reported in the FeO, FeS, and $FeBr_2$ systems with Fe^{2+} octahedral local symmetry, in which the substantial orbital magnetic moment is 0.7–1.1 μ_B.[26] In order to investigate the size of the orbital moment, Fe-$L_{2,3}$ XMCD measurements were carried out (Figure 4b). The XMCD (blue line) is defined as the difference between the X-ray absorption spectra taken with the photon spin of the circular polarized light parallel (black line) and antiparallel (red line) when aligned to the magnetic field. The large difference in the dichroic signal between the L_3 and L_2 edges in Figure 4b is a clear sign that the Fe^{2+} ions have a significant unquenched orbital moment. The collected XMCD signal can be quantitatively analyzed by means of the sum rules,[27,28] which provide the ratio

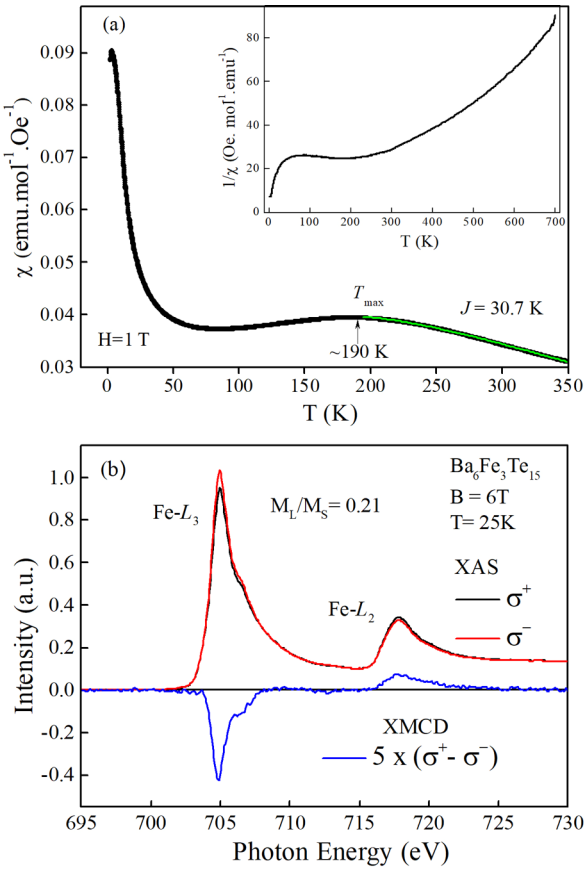

Figure 4. (a) Temperature dependence of susceptibility for $Ba_9Fe_3Te_{15}$ measured at a magnetic field of 1 T. The inset shows the temperature dependence of inverse susceptibility with a temperature range from 2 to 700 K; the green line is a fitting according to the Wagner–Friedberg model. (b) XMCD of Fe-$L_{2,3}$ edges for $Ba_9Fe_3Te_{15}$. The photon spin of the circular polarized light is aligned parallel (σ^+, black line) and antiparallel (σ^-, red line) to the applied magnetic field. The XMCD spectrum is shown in blue.

$$\frac{L_z}{2S_z + 7T_z} = \frac{2}{3}\frac{\int_{L_{2,3}}(\sigma^+ - \sigma^-)\mathrm{d}E}{\int_{L_3}(\sigma^+ - \sigma^-)\mathrm{d}E - 2\int_{L_2}(\sigma^+ - \sigma^-)\mathrm{d}E}$$

where the σ^+ and σ^- indicate the photon spin parallel and antiparallel to the applied field, respectively. For ions with octahedral symmetry, the intra-atomic magnetic dipole moment T_z is a small number and can be neglected compared to S_z.[29] Using the formula above, we obtained an orbital to spin moment ratio, $L_z/2S_z$, equal to 0.21, and thereby the orbital moment is estimated to be ~0.84 μ_B per Fe. Such a large orbital moment is comparable to the theoretical calculated orbital moment of 0.80 μ_B per Fe in hexagonal $FeBr_2$.[26]

Besides the nonlinear relationship of $1/\chi \sim T$, the susceptibility curve shows a hump with the maximum susceptibility at 190 K (T_{max}) as the temperature decreases, followed by a sharp rise at low temperatures as shown in Figure 4a. Generally, the broad hump-like feature is indicative of low-dimensional short-range magnetic correlation, which should derive from the short-range antiferromagnetic correlation associated with the intrachain interaction (J_{intra}) in the quasi-1D $Ba_9Fe_3Te_{15}$; this is similar to that in other quasi-1D systems,[30] such as Ba_2FeS_3, Ba_2CoS_3, and Ba_2MnS_3, and two-dimensional systems, such as $(Ba,Sr)_4Mn_3O_{10}$.[31] The magnetic

https://dx.doi.org/10.1021/acs.inorgchem.9b03592
Inorg. Chem. 2020, 59, 5377–5385

susceptibilities in the high-temperature region $T > T_{max}$ can be described according to the Wagner−Friedberg model. Wagner and Friedberg extended the Fisher model to the case of spin values different from 1/2 with the following formula[32]

$$\chi = \frac{N\mu_B{}^2 g^2 S(S+1)}{3k_B T} \frac{1 - U(T_0/T)}{1 + U(T_0/T)}$$

where $T_0 = 2J_{intra}S(S+1)$, $U(x) = \coth(x) - \frac{1}{x}$, g is the Landé constant, N is the Avogadro constant, S is the spin moment, and J_{intra} is the intrachain interaction.[32,33] Here, J_{intra} for the antiferromagnetic coupling is defined as negative. It should be noted that the Wagner−Friedberg model cannot be used to fit the low-temperature region where $T < T_{max}$. After fitting to the high-temperature susceptibility ($T > T_{max}$), presented in Figure 4a as a green line, the obtained intrachain coupling J_{intra} is about −31 K. Also, we can estimate the J_{intra} values via the mean-field approximation with the equation $k_B\theta = \frac{2z}{3}(S(S+1))J$, where θ is the temperature associated with the intrachain coupling strength and can be roughly replaced with the maximum temperature T_{max}, z is the number of nearest neighbors involved in the exchange coupling ($z = 2$ for the intrachain coupling), and $S = 2$ is the spin moment for Fe^{2+}. Thus, the values of J_{intra} can be calculated to be about −24 K. Because of the strong magnetic fluctuation in quasi-1D spin chains, the value of θ is underestimated if T_{max} is used here. Therefore, the intrachain interaction obtained from mean-field approximation is somewhat lower than that from the Wagner−Friedberg model.

In order to clarify the magnetic behavior at low temperatures, the ZFC and FC processes were measured at the low field of 100 Oe, as shown in Figure 5. The sharp increase in

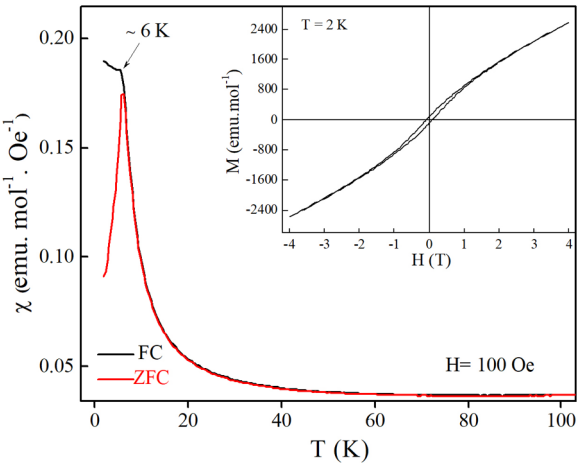

Figure 5. ZFC and FC dc magnetization plots for $Ba_9Fe_3Te_{15}$ measured at the applied magnetic field, H = 100 Oe. The inset shows the field dependence of the magnetization measured at 2 K for $Ba_9Fe_3Te_{15}$.

both the ZFC and FC curves below 20 K shows a paramagnetic (PM) to ferromagnetic-like (FM) transition. On further cooling, the ZFC magnetization curve diverges from the FC curve at the irreversibility temperature ($T_{irr} \approx 6$ K) and exhibits a peak at temperature T_p while the FC magnetization curve continues to grow, albeit at a slower rate. Generally, this type of temperature dependence of the magnetic irreversibility is observed in spin glass,[34] cluster glass,[35] super spin glass,[36] super paramagnets,[37] and anisotropic ferromagnets.[38,39] Since the structure of $Ba_9Fe_3Te_{15}$ is noncentrosymmetric, the Dzyaloshinskii−Moriya (DM) interaction usually contributes to the magnetism and leads to a canted spin arrangement. Therefore, the weak ferromagnetism derived from the spin canting is possible in $Ba_9Fe_3Te_{15}$. Further, it is noted that the magnetic signals with very small orders of magnitude for both the dc and ac susceptibility (see Figure 6), the isothermal magnetization at 2 K with little

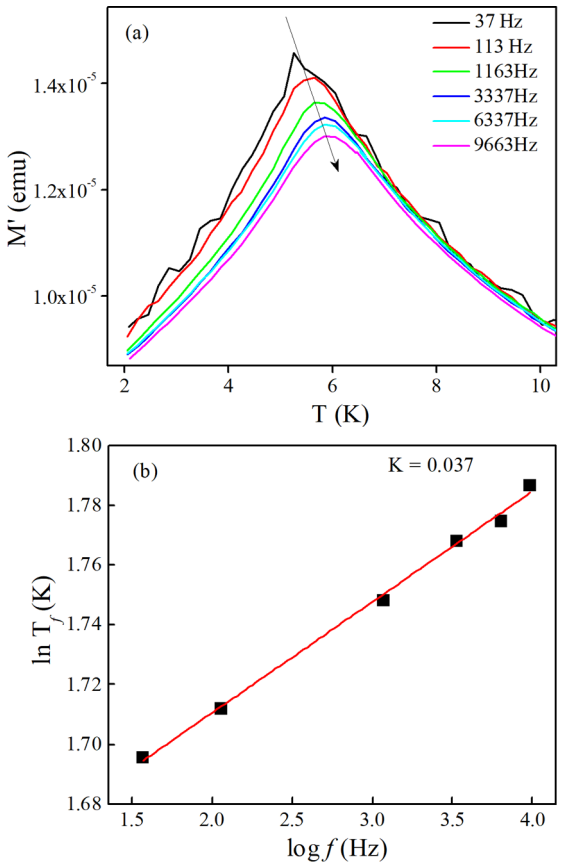

Figure 6. Plots for the ac magnetic properties of $Ba_9Fe_3Te_{15}$: (a) the real part of the ac magnetization measured with representative frequencies and (b) the relationship between frequency and freezing temperature, which is fitted by the spin glass dynamic formula as the red line.

magnetic hysteresis, and the absence of a saturation moment all are not seriously compatible with an FM state. The super paramagnets are usually observed in certain nanomaterials and are caused by the size effect, such as nanowire VO_2.[37] Therefore, it was reasonably deduced that the observed magnetic irreversibility may originate from the dynamic evolution of a spin glass state. The spin glass-like magnetic behavior that derives from strong frustration can be understood by a random distribution of spin at the triangular lattice that gives rise to a ferromagnetic and antiferromagnetic competition between the inter- and intrachains, as reported in the $Ba_9V_3Se_{15}$ system.[19] As for this, it is mainly influenced by the large distance between the adjacent chains due to the large Te atoms, and so the ferromagnetic interaction between the interchains could dominate because of the decreased radius for the coordinated atom, such as the S atom, in order to realize a

https://dx.doi.org/10.1021/acs.inorgchem.9b03592
Inorg. Chem. 2020, 59, 5377−5385

magnetoelectric effect in this noncentrosymmetrical system, such as a ferroelectricity application.

In order to elucidate the magnetic dynamics, the temperature dependence of ac magnetization was measured at various frequencies (f). The real (M') shown in Figure 6a and imaginary (M'') parts (Figure S1) exhibit peaks at 5.4−6.0 K, which is consistent with the freezing temperature observed in the dc susceptibility curves. In addition, the magnetic signals are rather weak; the intensity of the real part is 10^{-5} emu, whereas that of the imaginary part is about 10^{-7} emu. Nevertheless, it is still evident that the peak observed in real part (M'), centered at 5.4 K for the low frequency of 37 Hz, shifts toward the high-temperature direction as the frequency increases. More concretely, the temperature shifts by $\Delta_T \approx 0.6$ K, with a frequency change between 37 and 9663 Hz curves. The frequency dispersion is a hallmark of SG-like dynamics. The frequency shift, K, is calculated to reflect the frequency dependence by the following equation

$$K \equiv \Delta T_f/[T_f\ \Delta\log(f)]$$

where T_f is the freezing temperature at each f. The obtained value of $K \approx 0.037$ (Figure 6b), which falls in the expected range of values (0.005−0.08) for a canonical SG system,[40] indicating a spin glass behavior instead of a magnetic ordering state in $Ba_9Fe_3Te_{15}$. As proposed, the larger Te atoms actually decrease the coupling interactions in the linear chain, causing an antiferromagnetic correlation that favors realizing superconductivity.

Further, thermodynamic measurements were performed and were expected to reveal some intrinsic physical properties in this 1D magnetic chain system. The specific heat data collected at both zero field and 1 T show an unobserved anomaly at the spin glass freezing temperature (see Figure 7), which is a general property of materials with quasi-1D chains. Because far above the 3D magnetic transition temperature, the short-range spin correlation was developed gradually in the 1D chains, it led to most of the magnetic entropy release. Thus, the entropy anomaly in the heat capacity corresponding to the 3D magnetic transition or spin glass transition is usually very small. Here, $Ba_9Fe_3Te_{15}$ is a typical quasi-1D antiferromagnetic chain and the susceptibility presents a broad hump at 190 K, hinting at the development of a short-range antiferromagnetic correlation. Therefore, it is reasonable that no anomaly was observed in the specific heat data. Since the short-range spin correlation was developed gradually far above the spin glass transition, the quasi-1D $Ba_9Fe_3Te_{15}$ can be considered as decoupled spin chains above the transition temperature. Thus, in order to study the properties of the 1D spin chain and avoid the effect of the spin glass transition, the analysis of the heat capacity was performed above the transition temperature (6 K), as shown in the inset of Figure 7. For a 1D antiferromagnetic chain, the magnetic contribution to the heat capacity is proportional to T.[41] Therefore, we use the formula $C = \alpha T + (\beta T^3 + \eta T^5)$ to deal with the heat capacity for $Ba_9Fe_3Te_{15}$ within 8−20 K, where the first term is the magnetic contribution and the last two terms are the phonon contributions. After the fitting, we obtained the coefficient α = 88.7 mJ/(mol·K^2). Since $Ba_9Fe_3Te_{15}$ is a semiconductor, the large contribution of αT should arise from the spin excitation in the 1D antiferromagntic chain. In addition, using the Wagner−Friedberg model, we obtained the intrachain coupling about −31 K from the magnetic susceptibility experiment. According to Bonner and Fisher's work, the heat capacity for a 1D AFM chain can be described by $C(T) = 0.35Nk(kT/|J|)$,[41] where N is the Avogadro constant, k is the Boltzmann constant, and J is the spin coupling. Here, using $|J|$ = 31 K, we can get the coefficient to be 94 mJ/(mol·K^2), which agrees well with the experimental value of about 89 mJ/(mol·K^2). Additionally, the Debye temperature (θ_D) of 137 K was obtained according to the formula $\theta_D = [(12/5)NR\pi^4/\beta]^{1/3}$.

Along with the study of the magnetic properties, the investigation of the electronic transport properties provided a complementary way to analyze the electronic correlation and the possible band configuration. Figure 8 gives the temperature dependence of the resistivity for the $Ba_9Fe_3Te_{15}$ polycrystalline sample. As the temperature decreases, the resistivity increases, thereby demonstrating a semiconducting behavior. The inset shows the linear fit to the curve of $\ln(\rho)$ vs the inverse of the temperature according to a thermal activation model, where the green line is the linear fit. For a law of type $\rho \propto e^{(\Delta_g/2k_BT)}$,

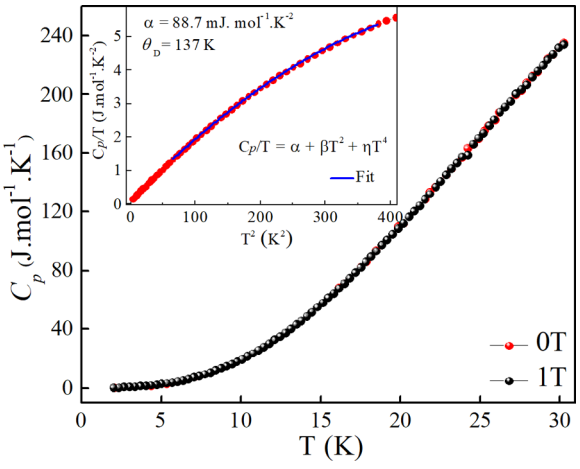

Figure 7. Heat capacity measurements under a 1 T field and no applied field for the $Ba_9Fe_3Te_{15}$. The inset shows the relationship between Cp/T and T^2. The blue line is the fit using the formula $C/T = \alpha + (\beta T^2 + \eta T^4)$ with a temperature range of 8−20 K, where α is the coefficient associated with the magnetic heat capacity and the second and third terms are the phonon contributions.

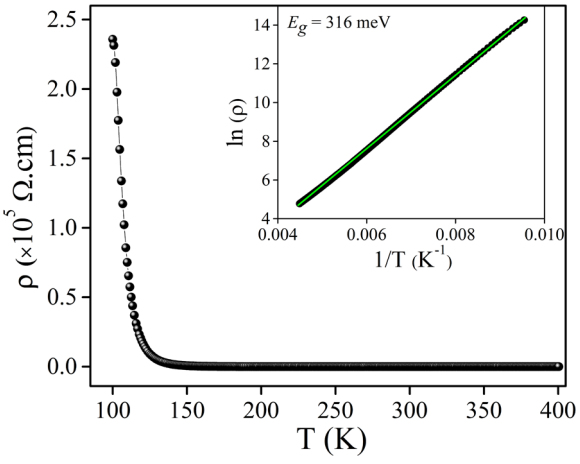

Figure 8. Electronic transport properties of the $Ba_9Fe_3Te_{15}$ polycrystalline sample. The inset shows the linear fit of resistivity using a thermal activation model yielding a band gap value of approximately 0.32 eV, where the green line is the fit curve.

https://dx.doi.org/10.1021/acs.inorgchem.9b03592
Inorg. Chem. 2020, 59, 5377−5385

where Δ_g is the semiconducting band gap and k_B is the Boltzmann constant, the resistivity curve can be well fitted and Δ_g is estimated to be 0.32 eV. Since $Ba_9Fe_3X_{15}$ has a much stronger 1D structure than $BaFe_2X_3$, the 3D conductivity in $Ba_9Fe_3X_{15}$ is mainly determined by the interchain electron hopping. In the $Ba_9Fe_3X_{15}$ system, when X varies from S to Te, the extension of the p orbital enhances the interchain electron hopping and thus increases the conductivity. For instance, the band gap decreases in the sequence of $Ba_9Fe_3S_{15}$ ($\Delta_g \approx 0.56$ eV),[11] $Ba_9Fe_3Se_{15}$ ($\Delta_g \approx 0.39$ eV),[17] and $Ba_9Fe_3Te_{15}$ ($\Delta_g \approx 0.32$ eV) and can be further tuned by doping or pressure. As reported for the 1D two-iron ladder iron chalcogenides $BaFe_2S_3$[5] and $BaFe_2Se_3$,[6] the insulating property was gradually depressed by pressure, and eventually the superconductivity emerged. Here, the difference for $Ba_9Fe_3Te_{15}$ is that the large distance between the adjacent $FeTe_6$ chains hinders the electron hopping, while doping or compression can in turn effectively tune the chain separation and enhance the individual chain coupling, resulting in a semiconductor-to-metal transition, or even superconductivity, as observed in the $BaFe_2S_3$ system.[4]

As a typical quasi-one-dimensional crystal, the $FeTe_6$ chain's sublattice in $Ba_9Fe_3Te_{15}$ is composed of $FeTe_6$ octahedra. Compared with the two-dimensional layered and two-legged ladder sublattice iron-based crystal, where the FeX_4 tetrahedra are considered to be the basic motifs, the $FeTe_6$ octahedral chains in this iron chalcogenide possess an antiferromagnetic exchange interaction as theoretically predicted for hexagonal FeTe[12] and are favored by superconductivity. The semiconductor behavior in $Ba_9Fe_3Te_{15}$ is similar to that in the 123-type iron chalcogenides, both of which originate from a chain-like crystal structure. According to the deduction that the superconductivity of $BaFe_2S_3$ is probably caused by the self-doping of electrons into the iron network, the critical pressure should be lower to suppress the magnetism and trigger the superconductivity because of the higher electron density of Fe, which derives from the strong covalent Fe−Te bond in $Ba_9Fe_3Te_{15}$, compared to other chalcogenides with similar structures. In addition, from a dimensionality perspective, the iron-based superconductors with a crystal structure evolving from layered to two-legged ladder types have emergent superconductivity at ambient pressures and at high application pressures as the structural dimensionality decreases. As expected, this quasi-one-dimensional chain featuring $Ba_9Fe_3Te_{15}$ may need a much higher critical pressure to increase the structural dimensionality and induce superconductivity. Overall, $Ba_9Fe_3Te_{15}$ represents an alternative type of iron-based compound, providing a diverse candidate for high-pressure studies in order to pursue some emerging physics.

4. CONCLUSION

A new iron-based compound $Ba_9Fe_3Te_{15}$, consisting of 1D $FeTe_6$ octahedral chains, was synthesized. Typical 1D antiferromagnetic characteristics, with a T_{max} at 190 K followed by a spin glass state at 6.0 K, and the insulating properties were unveiled, both of which seem closely related to the typical quasi-1D crystal structure. Furthermore, the unexpected orbital moment of ~0.84 μ_B per Fe was proven. The antiferromagnetic correlation and the small band gap in $Ba_9Fe_3Te_{15}$ favor the realization of superconductivity. The high-pressure work, including the pressure-induced structure transition, the spin-state crossover, the electronic transport, and even the superconductivity, will be great of interest for exploring the potential physics and understanding the fundamental underlying mechanism, which will be our next task of study.

■ ASSOCIATED CONTENT

Supporting Information

The Supporting Information is available free of charge at https://pubs.acs.org/doi/10.1021/acs.inorgchem.9b03592.

The imaginary part of the ac magnetization measured with representative frequencies for $Ba_9Fe_3Te_{15}$ (PDF)

■ AUTHOR INFORMATION

Corresponding Authors

Xiancheng Wang − *Beijing National Laboratory for Condensed Matter Physics, Institute of Physics, Chinese Academy of Sciences, Beijing 100190, China;* orcid.org/0000-0001-6263-4963; Email: wangxiancheng@iphy.ac.cn

Jinlong Zhu − *Center for High Pressure Science & Technology Advanced Research, Beijing 100094, People's Republic of China; Department of Physics, Southern University of Science and Technology, Shenzhen 518055, China*; Email: zhujl@sustech.edu.cn

Changqing Jin − *Beijing National Laboratory for Condensed Matter Physics, Institute of Physics, Chinese Academy of Sciences, Beijing 100190, China; School of Physics, University of Chinese Academy of Sciences, Beijing 100190, China; Songshan Lake Materials Laboratory, Dongguan 523808, China*; Email: jin@iphy.ac.cn

Authors

Jun Zhang − *Center for High Pressure Science & Technology Advanced Research, Beijing 100094, People's Republic of China; Beijing National Laboratory for Condensed Matter Physics, Institute of Physics, Chinese Academy of Sciences, Beijing 100190, China; School of Physics, University of Chinese Academy of Sciences, Beijing 100190, China;* orcid.org/0000-0002-9980-9074

Lei Duan − *Beijing National Laboratory for Condensed Matter Physics, Institute of Physics, Chinese Academy of Sciences, Beijing 100190, China; School of Physics, University of Chinese Academy of Sciences, Beijing 100190, China;* orcid.org/0000-0002-1254-0317

Zhe Wang − *College of Chemistry and Material Science, Hebei Normal University, Shijiazhuang 050024, China*

Jianfa Zhao − *Beijing National Laboratory for Condensed Matter Physics, Institute of Physics, Chinese Academy of Sciences, Beijing 100190, China; School of Physics, University of Chinese Academy of Sciences, Beijing 100190, China*

Meiling Jin − *Center for High Pressure Science & Technology Advanced Research, Beijing 100094, People's Republic of China*

Wenmin Li − *Beijing National Laboratory for Condensed Matter Physics, Institute of Physics, Chinese Academy of Sciences, Beijing 100190, China; School of Physics, University of Chinese Academy of Sciences, Beijing 100190, China*

Changling Zhang − *Beijing National Laboratory for Condensed Matter Physics, Institute of Physics, Chinese Academy of Sciences, Beijing 100190, China; School of Physics, University of Chinese Academy of Sciences, Beijing 100190, China*

Lipeng Cao − *Beijing National Laboratory for Condensed Matter Physics, Institute of Physics, Chinese Academy of Sciences, Beijing 100190, China*

https://dx.doi.org/10.1021/acs.inorgchem.9b03592
Inorg. Chem. 2020, 59, 5377−5385

Zheng Deng − *Beijing National Laboratory for Condensed Matter Physics, Institute of Physics, Chinese Academy of Sciences, Beijing 100190, China*
Zhiwei Hu − *Max Plank Institute for Chemical Physics of Solids, D-01187 Dresden, Germany*
Stefano Agrestini − *Max Plank Institute for Chemical Physics of Solids, D-01187 Dresden, Germany; ALBA Synchrotron Light Source, E-08290 Cerdanyola del Vallés, Barcelona, Spain*
Manuel Valvidares − *ALBA Synchrotron Light Source, E-08290 Cerdanyola del Vallés, Barcelona, Spain*
Hong-Ji Lin − *National Synchrotron Radiation Research Center (NSRRC), Hsinchu 30076, Taiwan*
Chien-Te Chen − *National Synchrotron Radiation Research Center (NSRRC), Hsinchu 30076, Taiwan*

Complete contact information is available at: https://pubs.acs.org/10.1021/acs.inorgchem.9b03592

Author Contributions

[▽]These authors contributed equally to this work.

Funding

We greatly appreciate the support of the National Key R&D Program of China and the Natural Science Foundation of China under grants 2018YFA0305700, 11974410, 2017YFA0302900, 2015CB921300, and 11534016. The work from HPSTAR was mainly supported by the National Natural Science Foundation of China (Grant U1530402). Jinlong Zhu was supported by the National Thousand-Young-Talents Program.

Notes

The authors declare no competing financial interest.

■ ACKNOWLEDGMENTS

All authors thank Ms. Freyja O'Toole for the proofreading of the manuscript. We acknowledge the support from the Max Planck-POSTECH-Hsinchu Center for Complex Phase Materials.

■ REFERENCES

(1) Wen, H. H.; Li, S. Materials and Novel Superconductivity in Iron Pnictide Superconductors. *Annu. Rev. Condens. Matter Phys.* **2011**, *2*, 121−140.
(2) Hsu, F. C.; Luo, J. Y.; Yeh, K. W.; Chen, T. K.; Huang, T. W.; Wu, P. M.; Lee, Y. C.; Huang, Y. L.; Chu, Y. Y.; Yan, D. C.; Wu, M. K. Superconductivity in the PbO-type structure α-FeSe. *Proc. Natl. Acad. Sci. U. S. A.* **2008**, *105* (38), 14262−14264.
(3) Ying, T. P.; Chen, X. L.; Wang, G.; Jin, S. F.; Lai, X. F.; Zhou, T. T.; Zhang, H.; Shen, S. J.; Wang, W. Y. Superconducting Phases in Potassium-Intercalated Iron Selenides. *J. Am. Chem. Soc.* **2013**, *135* (8), 2951−2954.
(4) Takahashi, H.; Sugimoto, A.; Nambu, Y.; Yamauchi, T.; Hirata, Y.; Kawakami, T.; Avdeev, M.; Matsubayashi, K.; Du, F.; Kawashima, C.; Soeda, H.; Nakano, S.; Uwatoko, Y.; Ueda, Y.; Sato, T. J.; Ohgushi, K. Pressure-induced superconductivity in the iron-based ladder material $BaFe_2S_3$. *Nat. Mater.* **2015**, *14* (10), 1008−1012.
(5) Yamauchi, T.; Hirata, Y.; Ueda, Y.; Ohgushi, K. Pressure-Induced Mott Transition Followed by a 24K Superconducting Phase in $BaFe_2S_3$. *Phys. Rev. Lett.* **2015**, *115* (11), 246402.
(6) Ying, J.; Lei, H.; Petrovic, C.; Xiao, Y.; Struzhkin, V. V. Interplay of magnetism and superconductivity in the compressed fe-ladder compound $BaFe_2Se_3$. *Phys. Rev. B: Condens. Matter Mater. Phys.* **2017**, *95* (24), 241109.
(7) Todorov, I.; Chung, D. Y.; Malliakas, C. D.; Li, Q. A.; Bakas, T.; Douvalis, A.; Trimarchi, G.; Gray, K.; Mitchell, J. F.; Freeman, A. J.; Kanatzidis, M. G. $CaFe_4As_3$: A Metallic Iron Arsenide with Anisotropic Magnetic and Charge-Transport Properties. *J. Am. Chem. Soc.* **2009**, *131* (15), 5405−5407.
(8) Hong, H. Y.; Steinfink, H. Crystal-Chemistry of Phases in Ba-Fe-S and Se Systems. *J. Solid State Chem.* **1972**, *5* (1), 93−104.
(9) Lei, H. C.; Ryu, H. J.; Frenkel, A. I.; Petrovic, C. Anisotropy in $BaFe_2Se_3$ single crystals with double chains of FeSe tetrahedra. *Phys. Rev. B: Condens. Matter Mater. Phys.* **2011**, *84* (21), 214511.
(10) Jenks, J. M.; Hoggins, J. T.; Rendondiazmiron, L. E.; Cohen, S.; Steinfink, H. Octahedrally coordinated iron in Ba-Fe-S system: $Ba_9Fe_3S_{11}(S_2)_2$, a high-pressure polymorph of Ba_3FeS_5. *Inorg. Chem.* **1978**, *17* (7), 1773−1775.
(11) Zhang, J.; Wang, X.; Duan, L.; Zhao, J.; Li, W.; Deng, Z.; Zhu, J.; Jin, C. Realization of the Magnetoelectric coupling in quasi one dimensional $Ba_9Fe_3S_{15}$. Submitted for publication 2020.
(12) Parker, D. S. Strong 3D and 1D magnetism in hexagonal Fe-chalcogenides FeS and FeSe vs. weak magnetism in hexagonal FeTe. *Sci. Rep.* **2017**, *7* (1), 3388.
(13) Zhang, Y.; Lin, L. F.; Zhang, J. J.; Dagotto, E.; Dong, S. Pressure-driven phase transition from antiferromagnetic semiconductor to nonmagnetic metal in the two-leg ladders AFe_2X_3 (A = Ba, K; X = S, Se). *Phys. Rev. B: Condens. Matter Mater. Phys.* **2017**, *95* (11), 115154.
(14) Mourigal, M.; Wu, S.; Stone, M. B.; Neilson, J. R.; Caron, J. M.; McQueen, T. M.; Broholm, C. L. Block Magnetic Excitations in the Orbitally Selective Mott Insulator$BaFe_2Se_3$. *Phys. Rev. Lett.* **2015**, *115* (4), 047401.
(15) Larson, A. C.; Von Dreele, R. B. General structure analysis system (GSAS). Los Alamos National Laboratory Report LAUR 86-748; 2000, pp 86−748.
(16) Barla, A.; Nicolas, J.; Cocco, D.; Valvidares, S. M.; Herrero-Martin, J.; Gargiani, P.; Moldes, J.; Ruget, C.; Pellegrin, E.; Ferrer, S. Design and performance of BOREAS, the beamline for resonant X-ray absorption and scattering experiments at the ALBA synchrotron light source. *J. Synchrotron Radiat.* **2016**, *23*, 1507−1517.
(17) Zhang, J.; Hao, Y.; Wang, X.; Liu, M.; Yang, Y.; Duan, L.; Jin, M.; Li, W.; Zhao, J. Z.; Cao, L.; Deng, Z.; Zhu, J.; Jin, C. $Ba_9Fe_3Se_{15}$: a helical ferromagnet with one dimensional spin chain. Submitted for publication 2020.
(18) Zhang, J.; Su, R.; Wang, X.; Li, W.; Zhao, J.; Deng, Z.; Zhang, S.; Feng, S.; Liu, Q.; Zhao, H.; Guan, P.; Jin, C. Synthesis, crystal structures, and electronic properties of one dimensional $Ba_9Sn_3(Te_{1-x}Se_x)_{15}$ (x = 0−1). *Inorg. Chem. Front.* **2017**, *4* (8), 1337−1343.
(19) Zhang, J.; Liu, M.; Wang, X.; Zhao, K.; Duan, L.; Li, W.; Zhao, J.; Cao, L.; Dai, G.; Deng, Z.; Feng, S.; Zhang, S.; Liu, Q.; Yang, Y.-f.; Jin, C. $Ba_9V_3Se_{15}$: a novel compound with spin chains. *J. Phys.: Condens. Matter* **2018**, *30*, 214001.
(20) Finlayson, D. M.; Greig, D.; Llewellyn, J. P.; Smith, T. Some Electrical Characteristics of Single Crystal Iron Monotelluride. *Proc. Phys. Soc., London, Sect. B* **1956**, *69* (8), 860−862.
(21) Brostigen, G.; Kjekshus, A. Compounds with the Marcasite Type Crystal-Structure. 5. Crystal Structure of FeS2, FeTe2 and CoTe2. *Acta Chem. Scand.* **1970**, *24* (6), 1925−1940.
(22) Burnus, T.; Hu, Z.; Wu, H.; Cezar, J. C.; Niitaka, S.; Takagi, H.; Chang, C. F.; Brookes, N. B.; Lin, H. J.; Jang, L. Y.; Tanaka, A.; Liang, K. S.; Chen, C. T.; Tjeng, L. H. X-ray absorption and x-ray magnetic dichroism study on Ca_3CoRhO_6 and Ca_3FeRhO_6. *Phys. Rev. B: Condens. Matter Mater. Phys.* **2008**, *77* (20), 205111.
(23) Hollmann, N.; Hu, Z.; Valldor, M.; Maignan, A.; Tanaka, A.; Hsieh, H. H.; Lin, H. J.; Chen, C. T.; Tjeng, L. H. Electronic and magnetic properties of the kagome systems $YBaCo_4O_7$ and $YBaCo_3MO_7$ (M = Al, Fe). *Phys. Rev. B: Condens. Matter Mater. Phys.* **2009**, *80* (8), 085111.
(24) Park, J. Electron spectroscopic study of 3d transition metal oxides and metal-insulator transitions. Ph.D. Thesis, University of Michigan, Ann Arbor, MI, 1994.
(25) Lai, K. T.; Adler, P.; Prots, Y.; Hu, Z.; Kuo, C.-Y.; Pi, T.-W.; Valldor, M. Successive Phase Transitions in Fe^{2+} Ladder Compounds

$Sr_2Fe_3Ch_2O_3$ (Ch = S, Se). *Inorg. Chem.* **2017**, *56* (20), 12606−12614.
(26) Radwanski, R. J.; Ropka, Z. Large orbital magnetic moment in FeO, FeS and FeBr2. *ActA Phys.* **2009**, *33*−*35*, 16−20.
(27) Thole, B. T.; Carra, P.; Sette, F.; Vanderlaan, G. X-Ray Circular-Dichroism as a Probe of Orbital Magnetization. *Phys. Rev. Lett.* **1992**, *68* (12), 1943−1946.
(28) Carra, P.; Thole, B. T.; Altarelli, M.; Wang, X. D. X-Ray Circular-Dichroism and Local Magnetic-Fields. *Phys. Rev. Lett.* **1993**, *70* (5), 694−697.
(29) Teramura, Y.; Tanaka, A.; Jo, T. Effect of Coulomb interaction on the X-ray magnetic circular dichroism spin sum rule in 3d transition elements. *J. Phys. Soc. Jpn.* **1996**, *65* (4), 1053−1055.
(30) Nakayama, N.; Kosuge, K.; Kachi, S.; Shinjo, T.; Takada, T. Studies on the Compounds in the Ba-Fe-S System. I. Linear Chain Antiferromagnetism of Ba_2FeS_3 and Related Compounds Ba_2CoS_3 and Ba_2MnS_3. *J. Solid State Chem.* **1980**, *33* (3), 351−356.
(31) Sannigrahi, J.; Chattopadhyay, S.; Bhattacharyya, A.; Giri, S.; Majumdar, S.; Venkateshwarlu, D.; Ganesan, V. Two dimensional magnetic correlation in the unconventional corrugated layered oxides $(Ba,Sr)_4Mn_3O_{10}$. *J. Phys.: Condens. Matter* **2015**, *27* (5), 056001.
(32) Barnes, A. D. J.; Baikie, T.; Hardy, V.; Lepetit, M. B.; Maignan, A.; Young, N. A.; Francesconi, M. G. Magnetic coupling and long-range order in the spin-chain sulfide Ba_2CoS_3. *J. Mater. Chem.* **2006**, *16* (34), 3489−3502.
(33) Wagner, G. R.; Friedberg, S. A. Linear Chain Antiferromagnetism in $Mn(HCOO)_2.2H_2O$. *Phys. Lett.* **1964**, *9* (1), 11−13.
(34) Mahana, S.; Topwal, D. Complex spin glass behavior in $Ga_{2-x}Fe_xO_3$. *Appl. Phys. Lett.* **2017**, *110* (10), 102907.
(35) Kumar, P. S. A.; Joy, P. A.; Date, S. K. Origin of the cluster-glass-like magnetic properties of the ferromagnetic system $La_{0.5}Sr_{0.5}CsO_3$. *J. Phys.: Condens. Matter* **1998**, *10* (29), L487−L493.
(36) Hiroi, K.; Komatsu, K.; Sato, T. Superspin glass originating from dipolar interaction with controlled interparticle distance among gamma-Fe_2O_3 nanoparticles with silica shells. *Phys. Rev. B: Condens. Matter Mater. Phys.* **2011**, *83* (22), 224423.
(37) Li, Z.; Guo, Y.; Hu, Z.; Su, J.; Zhao, J.; Wu, J.; Wu, J.; Zhao, Y.; Wu, C.; Xie, Y. Hydrogen Treatment for Superparamagnetic VO_2 Nanowires with Large Room-Temperature Magnetoresistance. *Angew. Chem., Int. Ed.* **2016**, *55* (28), 8018−8022.
(38) Kumar, D.; Rajeev, K. P.; Alonso, J. A.; Martínez-Lope, M. J. Spin-canted magnetism and decoupling of charge and spin ordering in $NdNiO_3$. *Phys. Rev. B: Condens. Matter Mater. Phys.* **2013**, *88* (1), 014410.
(39) Kumar, D.; Banerjee, A. Coexistence of interacting ferromagnetic clusters and small antiferromagnetic clusters in $La_{0.5}Ba_{0.5}CoO_3$. *J. Phys.: Condens. Matter* **2013**, *25* (21), 216005.
(40) Lekshmi, P. N.; Raji, G. R.; Vasundhara, M.; Varma, M. R.; Pillai, S. S.; Valant, M. Re-entrant spin glass behaviour and magneto-dielectric effect in insulating Sm_2NiMnO_6 double perovskite. *J. Mater. Chem. C* **2013**, *1* (40), 6565.
(41) Bonner, J. C.; Fisher, M. E. Linear Magnetic Chains with Anisotroyic Coupling. *Phys. Rev.* **1964**, *135* (3A), A640−A658.

https://dx.doi.org/10.1021/acs.inorgchem.9b03592
Inorg. Chem. 2020, 59, 5377−5385